Document Version
Final published version

Citation (APA)
Haakman, K., Slobbe, C., & Verlaan, M. (2025). Frequency Response Analysis of State Space Models for Time Series Analysis. *Earth and Space Science*, *12*(12), Article e2025EA004495. https://doi.org/10.1029/2025EA004495

Earth and Space Science

RESEARCH ARTICLE
10.1029/2025EA004495

Key Points:

- The frequency responses of several common state space models are derived
- The ratio of observation variance to disturbance variance fully determines the frequency response
- The frequency response provides interpretation of the noise variance parameters

Supporting Information:

Supporting Information may be found in the online version of this article.

Correspondence to:

K. Haakman,
k.b.haakman@tudelft.nl

Citation:

Haakman, K., Slobbe, C., & Verlaan, M. (2025). Frequency response analysis of state space models for time series analysis. *Earth and Space Science*, *12*, e2025EA004495. https://doi.org/10.1029/2025EA004495

Received 20 MAY 2025
Accepted 6 NOV 2025

Author Contributions:

Conceptualization: Koen Haakman
Formal analysis: Koen Haakman
Funding acquisition: Cornelis Slobbe, Martin Verlaan
Investigation: Koen Haakman
Methodology: Koen Haakman
Project administration: Cornelis Slobbe, Martin Verlaan
Software: Koen Haakman
Supervision: Cornelis Slobbe, Martin Verlaan
Visualization: Koen Haakman
Writing – original draft: Koen Haakman
Writing – review & editing: Koen Haakman, Cornelis Slobbe, Martin Verlaan

Frequency Response Analysis of State Space Models for Time Series Analysis

Koen Haakman[1], **Cornelis Slobbe**[1], **and Martin Verlaan**[2,3]

[1]Department of Geoscience and Remote Sensing, Delft University of Technology, Delft, The Netherlands, [2]Deltares, Delft, The Netherlands, [3]Department of Mathematical Physics, Delft University of Technology, Delft, The Netherlands

Abstract State space models are well-suited for time series in which the evolution of variables cannot be well represented by deterministic basis functions. A key challenge in using state space models is the selection of the noise variance parameters. To better understand their impact on the model's filtering behavior, we derive the frequency response of several commonly used state space models by utilizing the connection between the Kalman smoother and regularized least squares problems. We show that the frequency response reveals distinguishing spectral features between competing state space models and explains the flattening of the log-likelihood function when the ratio of observation to disturbance variance becomes large. Using Dutch tide gauge data, we illustrate how the frequency response can be used to make informed decisions about the variance parameters, which could in turn support more reliable interpretations of time series data.

1. Introduction

Many time series in Earth sciences exhibit nonstationary behavior. A common approach for analyzing such time series is the use of a state space model (SSM), also known as dynamic linear models. These methods are well-established in econometrics (e.g., Durbin & Koopman, 2012; Harvey, 1990), and are gaining traction in the geosciences, where they have been used to study time-varying seasonality in GNSS and GRACE data (Davis et al., 2012), time-varying trends in stratospheric ozone (Laine et al., 2014), mass changes in Antarctica (Willen et al., 2021) and time-varying trends in sea level (Frederikse et al., 2016; Steffelbauer et al., 2022; Visser et al., 2015).

State space models can be seen as a dynamic generalization of linear regression. In linear regression, unknown parameters are constant in time, leading to purely deterministic basis functions. In contrast, SSMs assume that the unknown parameters follow a stochastic process, allowing them to vary over time. This flexibility makes SSMs ideal for analyzing variables that change over time in ways that a simple functional relationship cannot capture.

The main challenge with the use of SSMs is that the variances of the stochastic processes must be prescribed. These variances control the extent to which parameters are allowed to vary over time. Typically, these variances are estimated using maximum likelihood estimation (MLE) (Durbin & Koopman, 2012). Sometimes, they are manually tuned through trial and error (e.g., Frederikse et al., 2016). The choice of variance parameters is crucial, as it significantly influences the temporal evolution of the estimated states, and different choices can lead to considerably different conclusions.

While MLE has solid theoretical foundations, the log-likelihood function can be flat near the optimum and may be sensitive to noise (e.g., Auger-Méthé et al., 2016; Chopin & Papaspiliopoulos, 2020). On the other hand, manually tuning the filter introduces a degree of subjectivity. In either case, the interpretation of the selected noise variance parameters is often unclear.

In this paper, we aim to provide a tool for understanding the impact of the noise variance parameters. Specifically, we explore the connection between state space models and digital filters. In signal processing, a widely used approach to tune filters is by analyzing their frequency response. The frequency response determines how the filter alters the amplitude and phase of signals as a function of frequency. We will derive the frequency response for several commonly used SSMs.

So far, frequency domain interpretation of SSMs have focused on computing the power spectral density of the transition equations (see the lower equation in Equation 1) (Harvey, 1990; Young et al., 1999). However, these derivations do not account for the actual solution to the SSM, and as a result, they cannot differentiate between the frequency domain properties of the Kalman filter and the Kalman smoother. The former computes optimal state estimates using only past observations, while the latter also incorporates future observations, leading to different frequency domain behavior.

We will specifically focus on the Kalman smoother, since in many applications involving observational time series for investigating Earth system processes, the data is used offline, meaning that all observations are already available. By leveraging the fact that the smoothed solution to an SSM can also be found by reformulating the SSM as a regularized least squares problem (Aravkin et al., 2014; Plasil, 2023), we will derive the frequency response for the Kalman smoother. This reformulation naturally leads to difference equations that characterize the filter's behavior and have a well-established connection to the frequency response. Finally, we will illustrate how this frequency response provides insight into the filtering behavior of SSMs by analyzing sea level data from Dutch tide gauges. This data provides an appropriate example because sea level changes result from multiple physical processes acting on different timescales. Frequency response analysis helps reveal which timescales contribute to the estimated sea level trend.

The paper is structured as follows. Section 2 reviews the connection between SSMs and regularized least squares problems. In Section 3, we derive the frequency response for several commonly used components of SSMs: trends modeled by (integrated) random walks and periodic components modeled with amplitudes following (integrated) random walks. These models were chosen as they provide natural stochastic generalizations from commonly used deterministic basis functions in linear regression and serve as the building blocks of more complex state space models. Section 4 discusses the impact of finite observation records on the realizable frequency response. Thereafter, we illustrate the utility of the frequency response by analyzing Dutch tide gauge data in Section 5. Finally, Section 6 presents the discussion and conclusions.

2. Kalman Smoother and Least Squares

2.1. First Order State Space Model

Throughout, boldface letters denote vectors and matrices. We consider the linear Gaussian state space model:

$$\begin{aligned} \mathbf{y}_k &= \mathbf{H}_k\mathbf{x}_k + \boldsymbol{\varepsilon}_k, \qquad && \boldsymbol{\varepsilon}_k \sim N(0, \mathbf{R}_k), && \\ \mathbf{x}_{k+1} &= \mathbf{F}_k\mathbf{x}_k + \boldsymbol{\eta}_k, \qquad && \boldsymbol{\eta}_k \sim N(0, \mathbf{Q}_k), && \text{for } k = 1\ldots N, \end{aligned} \tag{1}$$

where

$\mathbf{y}_k :=$ observation vector $\qquad \mathbf{H}_k :=$ observation matrix
$\mathbf{x}_k :=$ state vector $\qquad \mathbf{F}_k :=$ transition matrix
$\boldsymbol{\varepsilon}_k :=$ observation noise $\qquad \mathbf{R}_k :=$ observation covariance matrix
$\boldsymbol{\eta}_k :=$ disturbance noise $\qquad \mathbf{Q}_k :=$ disturbance covariance matrix

The smoothing problem is concerned with finding the optimal estimate $\hat{\mathbf{x}}_k$ of the state vector $\mathbf{x}_k$ given all measurements $\mathbf{y}_1\ldots\mathbf{y}_N$. The solution is usually found recursively by applying the Kalman filter and smoother. However, the solution can also be found in a non-recursive manner by first formulating the smoothing problem as an optimization problem with the following objective function (Rauch et al., 1965):

$$\min_{\mathbf{x}_1\ldots\mathbf{x}_k} L = \sum_{k=1}^{N} \|\mathbf{y}_k - \mathbf{H}_k\mathbf{x}_k\|^2_{\mathbf{R}_k^{-1}} + \sum_{k=2}^{N} \|\mathbf{x}_k - \mathbf{F}_k\mathbf{x}_{k-1}\|^2_{\mathbf{Q}_k^{-1}}, \tag{2}$$

where $\|\mathbf{x}\|^2_{\mathbf{W}} = \mathbf{x}^\top\mathbf{W}\mathbf{x}$ and $\mathbf{W}$ represents an inverse covariance matrix. Following Aravkin et al. (2014), we combine vectors and matrices from individual time steps into concatenated vectors and block matrices:

$$\mathbf{x} = \mathrm{vec}(\mathbf{x}_1, \mathbf{x}_2 \ldots \mathbf{x}_N), \tag{3}$$

$$\mathbf{y} = \mathrm{vec}\left(\mathbf{y}_1, \mathbf{y}_2 \ldots \mathbf{y}_N\right), \tag{4}$$

$$\mathbf{H} = \operatorname{diag}(\mathbf{H}_1, \mathbf{H}_2 \ldots \mathbf{H}_N), \tag{5}$$

$$\mathbf{R} = \operatorname{diag}(\mathbf{R}_1, \mathbf{R}_2 \ldots \mathbf{R}_N), \tag{6}$$

$$\mathbf{Q} = \operatorname{diag}(\mathbf{Q}_1, \mathbf{Q}_2 \ldots \mathbf{Q}_N). \tag{7}$$

To combine the transition equations, we move $\mathbf{F}_k\mathbf{x}_k$ to the left-hand side of Equation 1, leaving only the noise term on the right-hand side, which we aim to minimize. We then stack all the transition equations together to form a single combined transition matrix:

$$\mathbf{F} = \begin{bmatrix} \mathbf{I} & & & & \\ -\mathbf{F}_1 & \mathbf{I} & & & \\ & -\mathbf{F}_2 & \mathbf{I} & & \\ & & \ddots & \ddots & \\ & & & -\mathbf{F}_{N-1} & \mathbf{I} \end{bmatrix}. \tag{8}$$

Now the objective function in Equation 2 can be reformulated as:

$$\min_{\mathbf{x}} L = \|\mathbf{y} - \mathbf{H}\mathbf{x}\|^2_{\mathbf{R}^{-1}} + \|\mathbf{F}\mathbf{x}\|^2_{\mathbf{Q}^{-1}}. \tag{9}$$

The first term reflects the usual least squares objective function, while the second term serves as a regularizer induced by the transition equations. By setting the gradient of Equation 9 to zero, we obtain the following equations that define the solution:

$$\left(\mathbf{H}^\top\mathbf{R}^{-1}\mathbf{H} + \mathbf{F}^\top\mathbf{Q}^{-1}\mathbf{F}\right)\hat{\mathbf{x}} = \mathbf{H}^\top\mathbf{R}^{-1}\mathbf{y}, \tag{10}$$

where $\hat{\mathbf{x}}$ denotes the smoothed estimate of the state vector. The matrix $\left(\mathbf{H}^\top\mathbf{R}^{-1}\mathbf{H} + \mathbf{F}^\top\mathbf{Q}^{-1}\mathbf{F}\right)$ has a symmetric block tridiagonal structure, that is,

$$\mathbf{H}^\top\mathbf{R}^{-1}\mathbf{H} + \mathbf{F}^\top\mathbf{Q}^{-1}\mathbf{F} = \begin{bmatrix} \mathbf{A}_1 & \mathbf{B}_1^\top & & \\ \mathbf{B}_1 & \mathbf{A}_2 & \mathbf{B}_2^\top & \\ & \ddots & \ddots & \ddots \\ & & \mathbf{B}_{N-1} & \mathbf{A}_N \end{bmatrix}, \tag{11}$$

where

$$\mathbf{A}_k = \mathbf{Q}_k^{-1} + \mathbf{F}_k^\top\mathbf{Q}_{k+1}^{-1}\mathbf{F}_k + \mathbf{H}_k^\top\mathbf{R}_k^{-1}\mathbf{H}_k, \tag{12}$$

$$\mathbf{B}_k = -\mathbf{Q}_{k+1}^{-1}\mathbf{F}_k. \tag{13}$$

Apart from the first and the last row, the rows of the matrix thus define the following set of difference equations:

$$\mathbf{B}_{k-1}\hat{\mathbf{x}}_{k-1} + \mathbf{A}_k\hat{\mathbf{x}}_k + \mathbf{B}_k^\top\hat{\mathbf{x}}_{k+1} = \mathbf{H}_k^\top\mathbf{R}_k^{-1}\mathbf{y}_k. \tag{14}$$

We consider the measurements $\mathbf{y}_k$ to be the input and the smoothed state vector $\hat{\mathbf{x}}_k$ to be the output. Since the output at time step k depends on the output at other time steps, the smoother is an Infinite Impulse Response (IIR) filter. It is well known that such difference equations can be used to derive a filter's frequency response (e.g., Chapter 5, Oppenheim & Schafer, 1999). In Section 3, we show what these difference equations look like for several common state space models and how they lead to the frequency response for those models.

2.2. Second Order State Space Model

In some state space models, like the integrated random walk model, the transition equations depend on states from more than one time step in the past. In practice, this is usually dealt with by augmenting the state vector with states from previous time steps. However, this leads to deterministic transition equations which do not readily fit in the optimization framework provided by Equation 9. Hence, for our analysis, it is more convenient to define a transition matrix for each past time step, that is,

$$\mathbf{x}_{k+1} = \mathbf{F}_k \mathbf{x}_k + \mathbf{G}_k \mathbf{x}_{k-1} + \boldsymbol{\eta}_k, \tag{15}$$

Now the combined transition matrix for the least squares interpretation is:

$$\mathbf{F} = \begin{bmatrix} \mathbf{I} & & & & \\ -\mathbf{F}_1 & \mathbf{I} & & & \\ -\mathbf{G}_2 & -\mathbf{F}_2 & \mathbf{I} & & \\ & \ddots & \ddots & \ddots & \\ & & -\mathbf{G}_{N-1} & -\mathbf{F}_{N-1} & \mathbf{I} \end{bmatrix}. \tag{16}$$

In this case, the matrix $\left(\mathbf{H}^\top \mathbf{R}^{-1}\mathbf{H} + \mathbf{F}^\top \mathbf{Q}^{-1}\mathbf{F}\right)$ has a symmetric block pentadiagonal structure, that is,

$$\mathbf{H}^\top \mathbf{R}^{-1}\mathbf{H} + \mathbf{F}^\top \mathbf{Q}^{-1}\mathbf{F} = \begin{bmatrix} \mathbf{A}_1 & \mathbf{B}_1^\top & \mathbf{C}_1^\top & & \\ \mathbf{B}_1 & \mathbf{A}_2 & \mathbf{B}_2^\top & \mathbf{C}_2^\top & \\ \mathbf{C}_2 & \mathbf{B}_2 & \mathbf{A}_3 & \mathbf{B}_3^\top & \mathbf{C}_3^\top \\ & \ddots & \ddots & \ddots & \ddots \\ & & \mathbf{C}_{N-1} & \mathbf{B}_{N-1} & \mathbf{A}_N \end{bmatrix}, \tag{17}$$

where

$$\mathbf{A}_k = \mathbf{Q}_k^{-1} + \mathbf{F}_k^\top \mathbf{Q}_{k+1}^{-1}\mathbf{F}_k + \mathbf{G}_{k+1}^\top \mathbf{Q}_{k+2}^{-1}\mathbf{G}_{k+1} + \mathbf{H}_k^\top \mathbf{R}_k^{-1}\mathbf{H}_k, \tag{18}$$

$$\mathbf{B}_k = -\mathbf{Q}_{k+1}^{-1}\mathbf{F}_k + \mathbf{F}_{k+1}^\top \mathbf{Q}_{k+2}^{-1}\mathbf{G}_{k+1}, \tag{19}$$

$$\mathbf{C}_k = -\mathbf{Q}_{k+2}^{-1}\mathbf{G}_{k+1}. \tag{20}$$

Except for the first and last two rows, the remaining rows of the matrix now represent the following difference equations:

$$\mathbf{C}_{k-1}\hat{\mathbf{x}}_{k-2} + \mathbf{B}_{k-1}\hat{\mathbf{x}}_{k-1} + \mathbf{A}_k\hat{\mathbf{x}}_k + \mathbf{B}_k^\top \hat{\mathbf{x}}_{k+1} + \mathbf{C}_k^\top \hat{\mathbf{x}}_{k+2} = \mathbf{H}_k^\top \mathbf{R}_k^{-1}\mathbf{y}_k. \tag{21}$$

These difference equations again characterize the filtering behavior of the state space model and can be used to derive the frequency response of second order state space models.

3. Frequency Response Derivations for Common SSMs

3.1. Random Walk

In this section, we consider a state space model that consists of a random walk (RW) plus noise. It is also often referred to as the local level model. It is given by:

$$\begin{aligned} y_k &= \mu_k + \varepsilon_k, \qquad && \varepsilon_k \sim N\left(0, \sigma_\varepsilon^2\right), \\ \mu_{k+1} &= \mu_k + \eta_k, \qquad && \eta_k \sim N\left(0, \sigma_\eta^2\right). \end{aligned} \tag{22}$$

In the notation of Equation 1, we thus have $\mathbf{x}_k = \mu_k$, $\mathbf{H}_k = \mathbf{F}_k = [1]$, $\mathbf{R}_k = \sigma_\varepsilon^2$, $\mathbf{Q}_k = \sigma_\eta^2$. Substitution of these variables into Equation 14 yields the following difference equation:

$$-\frac{1}{\sigma_\eta^2}\hat{\mu}_{k-1} + \left(\frac{2}{\sigma_\eta^2} + \frac{1}{\sigma_\varepsilon^2}\right)\hat{\mu}_k - \frac{1}{\sigma_\eta^2}\hat{\mu}_{k+1} = \frac{y_k}{\sigma_\varepsilon^2}. \tag{23}$$

This equation was previously derived by Whittle (1991), and in principle, could be used directly to compute the smoothed solution to the RW model using appropriate initial conditions. However, as noted in Durbin and Koopman (2012; Section 4.6.3), the equation is numerically unstable.

For simplification, we multiply the equation by σ_ε^2 and define the noise variance ratio (NVR) $r = \sigma_\varepsilon^2/\sigma_\eta^2$. After reordering, we find:

$$\hat{\mu}_k = y_k + r\left(\hat{\mu}_{k-1} - 2\hat{\mu}_k + \hat{\mu}_{k+1}\right). \tag{24}$$

The term between parentheses on the right-hand-side corresponds to a central difference approximation of a second derivative. Suppose that this term is positive, then by Equation 24, $\hat{\mu}_k$ has to increase by an amount depending on the NVR, which in turn decreases the second derivative. Hence, in the random walk model, the NVR is responsible for penalizing the presence of a second derivative in the smoothed level $\hat{\mu}_k$. The difference equation can be used to derive the frequency response of the local level model by taking its Z-transform, which yields

$$M(z) = Y(z) + r\left(z^{-1}M(z) - 2M(z) + zM(z)\right), \tag{25}$$

where $M(z) = \mathcal{Z}\{\hat{\mu}[k]\}$ and $Y(z) = \mathcal{Z}\{y[k]\}$. Note that by taking the Z-transform without accounting for initial or final values, we implicitly assume that the difference equation extends indefinitely. In practice, with a finite amount of data, boundary effects cause the smoother weights to vary over time. Therefore, Equation 25 describes only the steady-state behavior of the Kalman smoother.

In order to find the frequency response, we first compute the transfer function. A transfer function relates a system's input to its output in the complex domain. In this case, we consider the measurements y_k as our input and the smoothed level $\hat{\mu}_k$ as our output. The transfer function then becomes

$$H(z) = \frac{M(z)}{Y(z)} = \frac{1}{1 + r(2 - (z^{-1} + z))}. \tag{26}$$

Evaluating the transfer function along the unit circle ($z = e^{j\omega}$) gives the following frequency response:

$$H\left(e^{j\omega}\right) = \frac{1}{1 + r(2 - 2\cos(\omega))}. \tag{27}$$

In Appendix D, we show that this equation can also be found from Wiener filtering theory, despite the fact that the random walk process is non-stationary, which violates a key assumption of the Wiener filter. Therefore, that approach by itself does not guarantee optimality of the derived frequency response. Moreover, the approach here

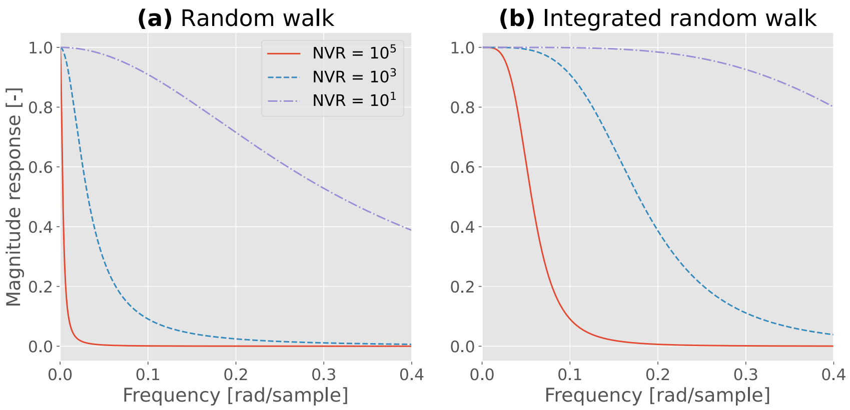

Figure 1. Magnitude responses of state space models consisting of a time-varying trend following a random walk (a) or an integrated random walk (b). The dash-dotted, dashed and solid lines correspond to noise variance ratios (NVR = $\sigma_\varepsilon^2/\sigma_\eta^2$) of 10^1, 10^3 and 10^5, respectively.

provides additional insight into the behavior of an SSM by revealing the difference equations governing the smoothed solution.

From Equation 27, we can make several observations. First, note that the frequency response depends only on the NVR, here represented by r. This parameter fully determines the behavior of the filter: if $r \to 0$, the frequency response tends to unity, corresponding to an all-pass filter. For large r, the frequency response first tends to a delta peak at the zero frequency, after which it eventually decays to zero completely.

Second, since the frequency response is real-valued, the phase response is zero, meaning the filter introduces no phase distortions. We will see that this property holds for all frequency responses derived in this paper. However, while this property holds for the Kalman smoother, it does not hold for the Kalman filter. Since the Kalman filter is causal, its impulse response is asymmetric in time. As a result, the frequency response, given by the Fourier transform of the impulse response, has a nonzero imaginary part, leading to a nonzero phase response.

Third, we note that $2 - 2\cos(\omega)$ is the discrete-time Fourier transform of the 3-point central approximation to the second derivative, that is,

$$\mathcal{F}\big(\hat{\mu}_{k-1} - 2\hat{\mu}_k + \hat{\mu}_{k+1}\big) = (2 - 2\cos(\omega))M(\omega). \tag{28}$$

Therefore, since the frequency response divides by the second derivative in the frequency domain, we can interpret the frequency response as an integrator or a low-pass filter.

In Figure 1a, the frequency response is visualized for three values of the noise variance ratio. As expected, the random walk model attenuates high-frequency components while letting low-frequency signals pass through. The NVR determines the rate at which the frequency response decreases, with a higher NVR leading to a more rapid decay.

3.2. Integrated Random Walk

In this section, we consider the state space model in which the trend is modeled by an integrated random walk (IRW), sometimes also referred to as the local linear trend model. An IRW is a stochastic process defined by

$$\Delta^2\mu_k = \eta_k, \tag{29}$$

where Δ^2 denotes the second-order backward difference operator:

$$\Delta^2\mu_k = \mu_k - 2\mu_{k-1} + \mu_{k-2}. \tag{30}$$

We hence consider the following state space model:

$$\begin{aligned} y_k &= \mu_k + \varepsilon_k, & \varepsilon_k &\sim N(0,\sigma_\varepsilon^2), \\ \mu_{k+1} &= 2\mu_k - \mu_{k-1} + \eta_k, & \eta_k &\sim N(0,\sigma_\eta^2). \end{aligned} \tag{31}$$

The major difference with the random walk model is that the transition equation now depends on two previous time steps instead of one. In practice, this is dealt with by augmenting the state vector by another variable, $\nu_k = \mu_k - \mu_{k-1}$. This leads to a Markovian formulation of the IRW state space model:

$$\begin{aligned} y_k &= \mu_k + \varepsilon_k, & \varepsilon_k &\sim N(0,\sigma_\varepsilon^2), \\ \mu_{k+1} &= \mu_k + \nu_k, & & \\ \nu_{k+1} &= \nu_k + \eta_k, & \eta_k &\sim N(0,\sigma_\eta^2). \end{aligned} \tag{32}$$

For the purpose of this derivation, the first formulation in which the state depends on two previous time steps is most convenient. Let $\mathbf{x}_k = \mu_k$. Following the notation set in Section 2.2, we set $\mathbf{F}_k = [2]$ and $\mathbf{G}_k = [-1]$. The other matrices are the same as in the random walk case. Evaluating Equation 21 now yields a difference equation that can be formulated as:

$$\hat{\mu}_k = y_k - r\nabla^4\hat{\mu}_k, \tag{33}$$

where we define ∇^4 to be a central approximation to the fourth derivative:

$$\nabla^4\hat{\mu}_k = \hat{\mu}_{k-2} - 4\hat{\mu}_{k-1} + 6\hat{\mu}_k - 4\hat{\mu}_{k+1} + \hat{\mu}_{k+2}. \tag{34}$$

Hence, in the IRW model, the fourth derivative of the trend is penalized by the NVR, while in the RW model, the second derivative is penalized. The frequency response can be found as before, which yields

$$H\left(e^{j\omega}\right) = \frac{1}{1 + r[2 - 2\cos(\omega)]^2}. \tag{35}$$

Note that $[2 - 2\cos(\omega)]^2$ is the discrete-time Fourier transform of ∇^4. Hence, the frequency response can be interpreted as a higher order integrator than the RW frequency response. The magnitude response of this filter is plotted for various values of the noise variance ratio r in Figure 1b. It can be seen that the IRW filter has a larger spectral bandwidth compared to the RW filter for the same noise variance ratio. Moreover, the IRW filter is characterized by a flat top at low frequencies and it has a faster roll-off rate compared to the RW filter. Hence, the IRW model is closer to an ideal low-pass filter than the RW model. However, this does not imply that the IRW trend is always the more suitable choice. If the true signal exhibits substantial high-frequency variability, as is the case in for example, wind speed or precipitation time series, then the RW filter may provide a more appropriate representation than the IRW filter.

3.3. Periodic Component With RW Amplitude

In this section, we consider a state space model that includes only a single stochastic periodic component. One approach to model such a periodic component is to model it as a sum of a cosine and sine with amplitudes that follow a random walk. This gives rise to the following state space model:

$$\begin{aligned} y_k &= a_k\cos(\omega_0 t_k) + b_k\sin(\omega_0 t_k) + \varepsilon_k, & \varepsilon_k &\sim N(0,\sigma_\varepsilon^2), \\ a_{k+1} &= a_k + \eta_k, & \eta_k, \eta_k^* &\sim N(0,\sigma_\eta^2), \\ b_{k+1} &= b_k + \eta_k^*, & & \end{aligned} \tag{36}$$

where ω_0 is the fixed frequency of the periodic component. A disadvantage of the above model is that the observation matrix is time-varying due to presence of the $\cos(\omega_0 t_k)$ and $\sin(\omega_0 t_k)$ terms. A well-known alternative formulation follows from the following change of variables (e.g., Durbin & Koopman, 2012):

$$c_k = a_k \cos(\omega_0 t_k) + b_k \sin(\omega_0 t_k), \tag{37}$$

$$c_k^* = -a_k \sin(\omega_0 t_k) + b_k \cos(\omega_0 t_k), \tag{38}$$

where c_k denotes the total value of the periodic component at time step k and c_k^* is an unobserved auxiliary variable that is required for the recursive computation. The evolution of these variables can be modeled recursively which yields the following state space formulation:

$$\begin{aligned} y_k &= c_k + \varepsilon_k, & \varepsilon_k &\sim N\left(0, \sigma_\varepsilon^2\right), \\ c_{k+1} &= \cos(\tilde{\omega}_0)\, c_k + \sin(\tilde{\omega}_0)\, c_k^* + \eta_k, & \eta_k, \eta_k^* &\sim N\left(0, \sigma_\eta^2\right), \\ c_{k+1}^* &= -\sin(\tilde{\omega}_0)\, c_k + \cos(\tilde{\omega}_0)\, c_k^* + \eta_k^*, \end{aligned} \tag{39}$$

where $\tilde{\omega}_0 = \omega_0 \Delta t$ is the normalized frequency in radians per sample. As long as the disturbance variances for a_k, b_k, c_k and c_k^* are chosen equally, this model is equivalent to the model described in Equation 36 (Proietti, 2000). Since the recursive formulation yields time-invariant state matrices, it is easier to derive the frequency response from this formulation. Using the notation outlined in Section 2, we thus have:

$$\mathbf{x}_k = \begin{bmatrix} c_k & c_k^* \end{bmatrix}^\top, \tag{40}$$

$$\mathbf{H}_k = \begin{bmatrix} 1 & 0 \end{bmatrix}, \tag{41}$$

$$\mathbf{F}_k = \begin{bmatrix} \cos(\tilde{\omega}_0) & \sin(\tilde{\omega}_0) \\ -\sin(\tilde{\omega}_0) & \cos(\tilde{\omega}_0) \end{bmatrix}. \tag{42}$$

Substitution of the above variables into Equation 14 now gives two coupled difference equations, which can be put into the following form:

$$-r\cos(\tilde{\omega}_0)\left[\hat{c}_{k-1} + \hat{c}_{k+1}\right] - r\sin(\tilde{\omega}_0)\left[\hat{c}_{k-1}^* - \hat{c}_{k+1}^*\right] + (1+2r)\,\hat{c}_k = y_k, \tag{43}$$

$$\sin(\tilde{\omega}_0)\left[\hat{c}_{k-1} - \hat{c}_{k+1}\right] - \cos(\tilde{\omega}_0)\left[\hat{c}_{k-1}^* + \hat{c}_{k+1}^*\right] + 2\hat{c}_k^* = 0. \tag{44}$$

The second equation is homogeneous and can therefore be used to relate the Z-transform of $\hat{c}_k$ and $\hat{c}_k^*$. This relationship can be used to eliminate the Z-transform of $\hat{c}_k^*$ from Equation 43. Subsequently, the frequency response can be found as before. It is given by:

$$H\left(e^{j\omega}\right) = \frac{1}{1 + r\left[\frac{2(\cos(\omega) - \cos(\omega_0))^2}{1 - \cos(\omega_0)\cos(\omega)}\right]}. \tag{45}$$

The magnitude response is visualized in Figure 2a. As the NVR increases, the filter approaches a Dirac delta function centered on ω_0, which would be the frequency response of a deterministic harmonic in the context of standard linear regression. We note that although the frequency response is similar to a shifted version of the RW frequency response from Figure 1a, it is not exactly so. This discrepancy arises because, although the power spectral density (PSD) of the cyclic process is the sum of two shifted copies of the RW PSD (by the Fourier modulation property), the frequency response is a nonlinear function of the PSD, and thus not simply shifted.

3.4. Periodic Component With IRW Amplitude

In the previous section, the amplitudes of the sine and cosine were modeled as RWs. An alternative approach is to model the amplitudes as IRWs. This model has previously been explored in the context of dynamic harmonic regression (Young et al., 1999). An RW amplitude model is appropriate for capturing high-frequency variations in a periodic component, such as changes in ocean tides caused by river discharge or atmospheric forcing. In contrast, slower variations in ocean tides, for example, those induced by changes in ocean stratification (Opel

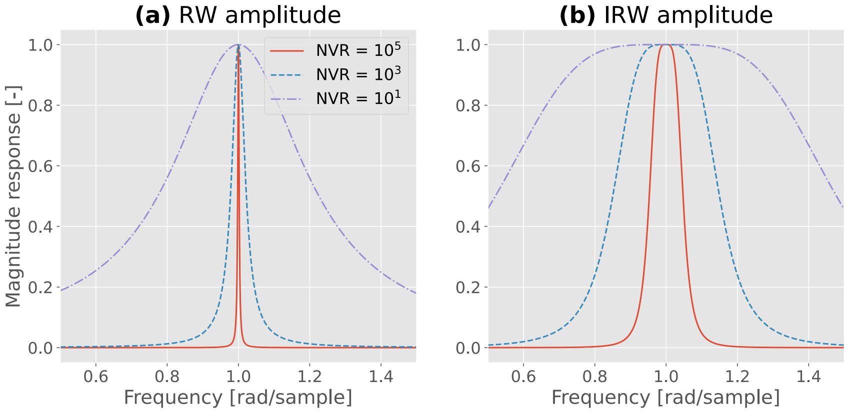

Figure 2. Magnitude responses of state space models consisting of a single stochastic periodic component. The amplitudes are modeled as random walks (a) or integrated random walks (b). The dash-dotted, dashed and solid lines correspond to noise variance ratios (NVR $= \sigma_\varepsilon^2/\sigma_\eta^2$) of 10^1, 10^3 and 10^5, respectively. The periodic component has a frequency of 1 radian per sample.

et al., 2024), may be better represented by a periodic component with IRW amplitudes, as this model naturally accommodates more gradual evolution over time. The corresponding state space formulation is given by:

$$\begin{aligned} y_k &= a_k\cos(\omega_0 t_k) + b_k\cos(\omega_0 t_k) + \varepsilon_k, & \varepsilon_k &\sim N(0,\sigma_\varepsilon^2),\\ a_{k+1} &= 2a_k - a_{k-1} + \eta_k, & \eta_k,\eta_k^* &\sim N(0,\sigma_\eta^2),\\ b_{k+1} &= 2b_k - b_{k-1} + \eta_k^*. \end{aligned} \tag{46}$$

The model has a time-varying observation matrix, which leads to time-varying difference equation describing the smoothed solution. As a result, the Z-transform cannot be applied directly. In Appendix A, we show how using a transformation of variables, these difference equations can be converted into a time-invariant form, allowing the frequency response of this model to be derived in a similar way as before. The frequency response is given by:

$$H(e^{j\omega}) = \frac{1}{1 + r\left[\frac{U(\omega)}{V(\omega)} - V(\omega)\right]}, \tag{47}$$

where

$$\begin{aligned} U(\omega) = {} & \sin^2(2\tilde{\omega}_0)(2 - 2\cos(4\omega))\\ & - 16\sin(\tilde{\omega}_0)\sin(2\tilde{\omega}_0)(\cos(\omega) - \cos(3\omega))\\ & - 16\sin^2(\tilde{\omega}_0)(2\cos(2\omega) - 2)), \end{aligned} \tag{48}$$

$$V(\omega) = 8\cos(\tilde{\omega}_0)\cos(\omega) - 2\cos(2\tilde{\omega}_0)\cos(2\omega) - 6. \tag{49}$$

The corresponding magnitude response is shown in Figure 2b for three different values of the noise variance ratio r. Clearly, the IRW amplitude model has a wider shape than the RW amplitude model with the same parameter. Moreover, the peak of the curve is much flatter in the IRW amplitude model. This may be a desirable feature in the context of time-varying periodic terms, as temporal modulations induce energy adjacent to the central frequency in the spectral domain. Note that by highlighting the distinct effects that each model has in the frequency domain, the frequency response can be used as a model selection tool.

3.5. Combination of Individual Components

So far, we have derived the frequency responses of simple state space models consisting of a single stochastic component. In practice, state space models often comprise of a sum of several of such components. In that case, there will be multiple frequency responses, one for each stochastic component of the model. These frequency responses can still be derived following the procedure from the previous sections.

We will here illustrate the consequences for a specific case: a model consisting of an IRW trend and a periodic term modeled recursively. This results in two frequency responses, one for the trend and one for the periodic term. We thus consider the following model:

$$\begin{aligned} y_k &= \mu_k + c_k + \varepsilon_k, & \varepsilon_k &\sim N(0, \sigma_\varepsilon^2), \\ \mu_{k+1} &= 2\mu_k - \mu_{k-1} + \eta_k, & \eta_k &\sim N(0, \sigma_\eta^2), \\ c_{k+1} &= \cos(\tilde{\omega}_0)\, c_k + \sin(\tilde{\omega}_0)\, c_k^* + \xi_k, & \xi_k, \xi_k^* &\sim N(0, \sigma_\xi^2), \\ c_{k+1}^* &= -\sin(\tilde{\omega}_0)\, c_k + \cos(\tilde{\omega}_0)\, c_k^* + \xi_k^*. \end{aligned} \tag{50}$$

Since the model contains two stochastic components, we now have two noise variance ratios:

$$r_\eta = \frac{\sigma_\varepsilon^2}{\sigma_\eta^2}, \qquad r_\xi = \frac{\sigma_\varepsilon^2}{\sigma_\xi^2}. \tag{51}$$

Let $C(z) = \mathcal{Z}\{\hat{c}[k]\}$. In Appendix B, we show that the frequency responses for the trend and cyclic term are respectively:

$$H_M\left(e^{j\omega}\right) = \frac{M\left(e^{j\omega}\right)}{Y\left(e^{j\omega}\right)} = \frac{1}{1 + r_\eta\left[\frac{\nabla^4\left(e^{j\omega}\right)}{r_\xi D\left(e^{j\omega}\right)} - \nabla^4\left(e^{j\omega}\right)\right]}, \tag{52}$$

$$H_C\left(e^{j\omega}\right) = \frac{C\left(e^{j\omega}\right)}{Y\left(e^{j\omega}\right)} = \frac{1}{1 + r_\xi\left[\frac{D\left(e^{j\omega}\right)}{r_\eta \nabla^4\left(e^{j\omega}\right)} - D\left(e^{j\omega}\right)\right]}, \tag{53}$$

where

$$D\left(e^{j\omega}\right) = 2\cos(\tilde{\omega}_0)\cos(\omega) - 2 + \frac{\sin^2(\tilde{\omega}_0)(2 - 2\cos(2\omega))}{2 - 2\cos(\tilde{\omega}_0)\cos(\omega)}, \tag{54}$$

$$\nabla^4\left(e^{j\omega}\right) = 8\cos(\omega) - 2\cos(2\omega) - 6. \tag{55}$$

In Figure 3, we visualize the two frequency responses under two scenarios: one where their spectra overlap significantly (top panel) and one where they are well separated in the frequency domain (bottom panel). In the top panel, the disagreement between the solid and dashed lines highlights that interaction effects are significant when the components spectrally overlap. In the bottom panel, the solid and dashed lines closely match, indicating negligible interaction. We conclude that when state space model components are well separated in the frequency domain, their individual frequency responses derived without accounting for interactions are adequate.

4. Windowed Frequency Response

So far, the frequency responses have been derived under the implicit assumption that an infinitely long time series is available. However, in practice, only a finite amount of data is available. The impact of this is most easily understood from the time domain. The time domain counterpart of the frequency response is the impulse response, which is obtained by applying the inverse Fourier transform to the frequency response. A narrow frequency response corresponds to a wide impulse response and vice versa. If the impulse response extends beyond the available time series length, it cannot be fully computed. Instead, a truncated impulse response is computed, which effectively corresponds to multiplying the infinite impulse response by a rectangular window in the time domain. Consequently, in the frequency domain, this corresponds to convolution of the frequency response with the Fourier transform of the rectangular window:

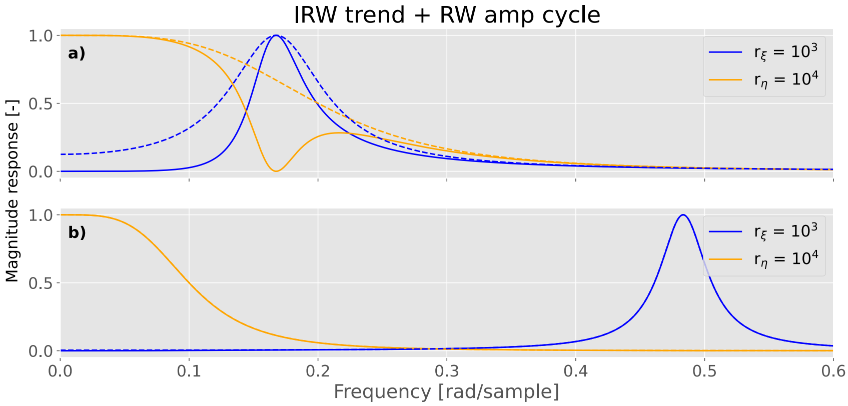

Figure 3. (a) Frequency responses of state space model consisting of two stochastic components: an integrated random walk (IRW) trend and a cyclic component with random walk (RW) amplitudes. Solid lines represent magnitude responses accounting for the interaction between the two components, whereas dashed lines show frequency responses that disregard this interaction. The orange lines correspond to the frequency response of the trend component, while the blue lines represent the frequency response of the periodic component. Panel (b) Same as in panel (a), but for a higher frequency periodic component such that the trend and periodic component do not overlap in the frequency domain.

$$H_{\mathrm{w}}\left(e^{j\omega}\right) = H\left(e^{j\omega}\right) * W(\omega), \tag{56}$$

where H_w denotes the windowed frequency response, the asterisk represents convolution and $W(\omega) = \sin(N\omega/2)/\sin(\omega/2)$ is the discrete-time Fourier transform of the rectangular window.

In Figure 4, we compare the analytical frequency response to numerically computed frequency responses for two values of the NVR. The numerical frequency responses are obtained by passing 10,000 white noise realizations of length $N = 1000$ through a state space model with a single periodic term with RW amplitudes.

In the left plot, the NVR r is smaller than in the right plot. This results in a wider spectral shape, corresponding to a shorter impulse response. Therefore, the truncation of the impulse response has minimal impact, which leads to close agreement between the orange and black lines. In contrast, the larger NVR in the right plot yields a narrower spectral shape, corresponding to a longer impulse response. As a result, truncation effects are more pronounced, leading to visible deviations between the orange and black lines.

In both plots, a small discrepancy remains between the blue and dashed orange lines, indicating a slight mismatch between the numerical and theoretical frequency responses. This difference is due to edge effects: near the

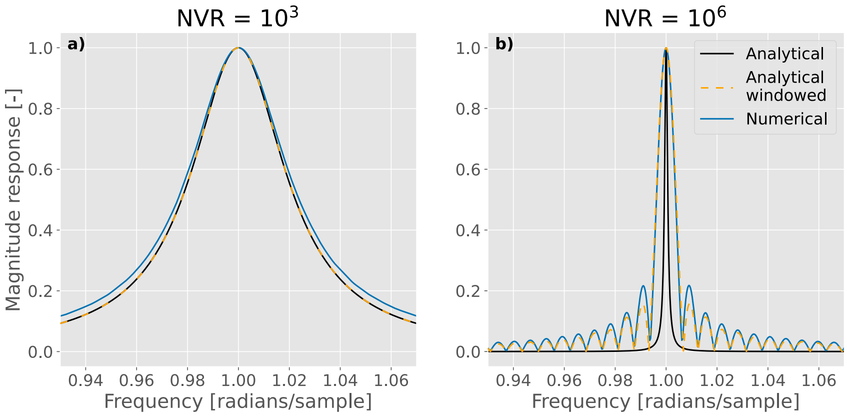

Figure 4. (a) Comparison of analytical, windowed and numerical frequency responses. The solid black lines represent the frequency response given by Equation 45 for a noise variance ratio (NVR) of 10^3. The dashed orange lines give the frequency response obtained by convolving the theoretical frequency response by the appropriate sinc function for $N = 1000$. The solid blue lines show the frequency response derived from numerical testing. Panel (b) Same as in panel (a), but for an NVR of 10^6.

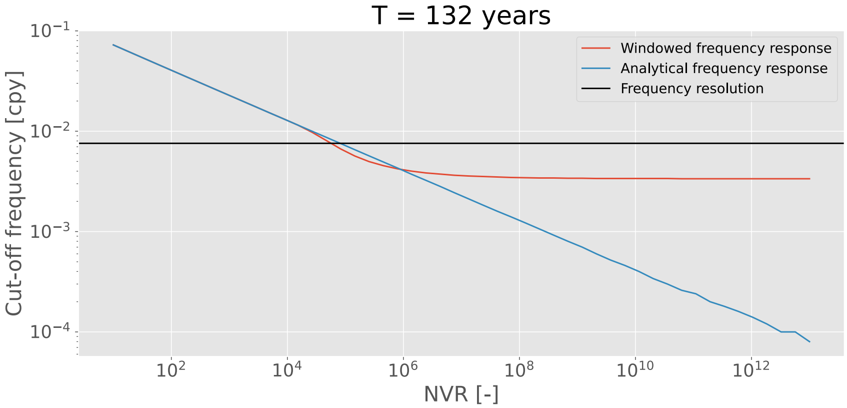

Figure 5. Cut-off frequency of the IRW trend frequency response as a function of the noise variance ratio (NVR $= \sigma_\varepsilon^2/\sigma_\eta^2$) when 132 years of data is available. The solid blue line corresponds to the analytical frequency response governed by Equation 35, while the solid red line take the finite data length into account following Equation 56. The horizontal black line indicates the frequency resolution.

boundaries of the time series, the optimal smoother weights differ from those in the center because only one-sided data is available. As a result, the smoother becomes time-varying, whereas the theoretical frequency response describes the steady-state behavior. Nevertheless, the deviations are minor, and the theoretical frequency responses still serve as a useful approximation.

Finally, we note that although the analytical frequency response can be made arbitrarily narrow by increasing the NVR, the windowed frequency response reaches a minimum width when it approaches the frequency resolution dictated by the observation record length. To quantify the width of the frequency response, we use the notion of the cut-off frequency of a filter, which is typically defined as the frequency where the input power is halved. Since the ratio of the output power to the input power is governed by the magnitude response squared, the cut-off frequency occurs at the point where the magnitude response is $1/\sqrt{2}$.

In Figure 5, the cut-off frequency for the IRW trend model is shown as a function of the NVR for an observation record spanning 132 years. The 132-year record length is motivated by the tide gauge case study in the next section. The blue lines show that the cut-off frequency can be made arbitrarily small by increasing the NVR, while the red lines indicate that, in practice, the cut-off frequency attains a minimum after which increasing the NVR does not further reduce the width of the frequency response. In the next section, we will see how this leveling off of the cut-off frequency can explain the flatlining of the log-likelihood functions which is often observed in practice (e.g., Auger-Méthé et al., 2016).

5. Application: Dutch Tide Gauge Data

To illustrate the utility of frequency response analysis, we will consider the problem of estimating time-varying trends of sea level at several Dutch tide gauges. Relative sea level, as measured by tide gauges, is influenced by many mechanisms acting on different timescales, including, but not limited to, thermal expansion, ice mass loss and associated gravitational effects, vertical land motion, tidal forces and atmospheric variability (Fox-Kemper et al., 2021; Pugh & Woodworth, 2014). Variability from atmospheric forcing is usually suppressed using a numerical model (e.g., Frederikse et al., 2016) or by including wind speed and air pressure time series as regressors (e.g., Frederikse & Gerkema, 2018). Tidal variability is largely averaged out by computing monthly or annual mean sea levels, while residual variability at the 18.6-year lunar nodal cycle can be accounted for by including sinusoidal regressors with this period.

We will here use the same data as in the Zeespiegelmonitor (Sea Level Monitor; Stolte et al., 2023), which is a report published every 4 years by Deltares that analyzes sea level changes to inform policymakers in the Netherlands. However, instead of using deterministic linear and quadratic functions, we will use an IRW to model the nonstationary trend. This stochastic approach is advantageous because it avoids assumptions about the shape of the trend and it eliminates the need to set a reference time for the acceleration term, which has a large influence on the estimated acceleration. Moreover, the IRW model is preferred over the RW model because its frequency

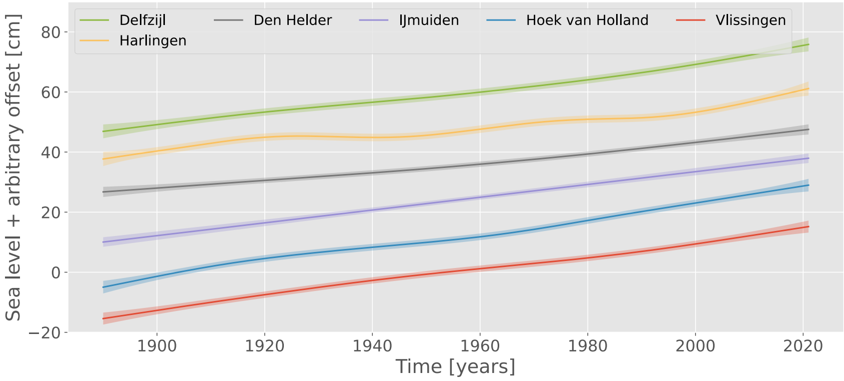

Figure 6. Time-varying trends at the six main Dutch tide gauges. The hyperparameters were fit using maximum likelihood estimation. The shaded areas provide the 95% confidence intervals.

response is more specific for the low frequency signals expected from the physical processes driving sea level changes at decadal timescales. The trade-off of the stochastic approach, however, is that it requires tuning the noise variance ratio of the IRW.

While we only illustrate the utility of the frequency response for the IRW here, the same principles apply to all other stochastic models considered in this study: their frequency responses can similarly be analyzed to understand how they filter variability across different timescales and to guide parameter selection.

5.1. Data

We use the yearly sea level heights from 1890 until 2021 at the six main Dutch tide gauges (see Figure 7a) provided by the Permanent Service for Mean Sea Level (PSMSL) (Holgate et al., 2013; PSMSL, 2025). To account for wind and air pressure effects, we follow Stolte et al. (2023) by removing modeled surface elevations from the Global Tide and Surge Model (GTSM; Muis et al. (2016)) after 1950. The mean surge between 1950 and 2022, which ranges from approximately 3–7 cm depending on the station, is removed from the data before 1950.

5.2. Model

We model the time series as a linear combination of an IRW trend and a deterministic periodic component at the frequency of the lunar nodal cycle. Since the residual errors of this model show significant autocorrelation at lag 1, we model the errors as an AR(1) process. Hence, we consider the following model:

$$\begin{aligned}
y_k &= \mu_k + c_k + \varepsilon_k, \\
\mu_{k+1} &= 2\mu_k - \mu_{k-1} + \eta_k, & \eta_k &\sim N\left(0, \sigma_\eta^2\right), \\
c_{k+1} &= \cos\left(\omega_{\text{nodal}}\Delta t\right) c_k + \sin\left(\omega_{\text{nodal}}\Delta t\right) c_k^*, \\
c_{k+1}^* &= -\sin\left(\omega_{\text{nodal}}\Delta t\right) c_k + \cos\left(\omega_{\text{nodal}}\Delta t\right) c_k^* \\
\varepsilon_{k+1} &= \phi\varepsilon_k + \xi_k, & \xi_k &\sim N\left(0, \sigma_\xi^2\right),
\end{aligned} \tag{57}$$

where ε_k represents the AR(1) noise, ϕ denotes the AR(1) parameter and $\Delta t = 1$ year. The model thus contains three hyperparameters: σ_ξ^2, σ_η^2 and ϕ.

5.3. Results

First, we determine the hyperparameters through maximum likelihood estimation. The resulting IRW trends are given in Figure 6. At first glance, all stations appear to show a similar rate of sea-level rise, although there is some difference in the amount of temporal variability in the trends between stations. In particular, the estimated trend at IJmuiden is exactly linear while there is some decadal variability at Harlingen. For a comparison of the estimated trends and the underlying observations, we refer to the figures in the supplementary information.

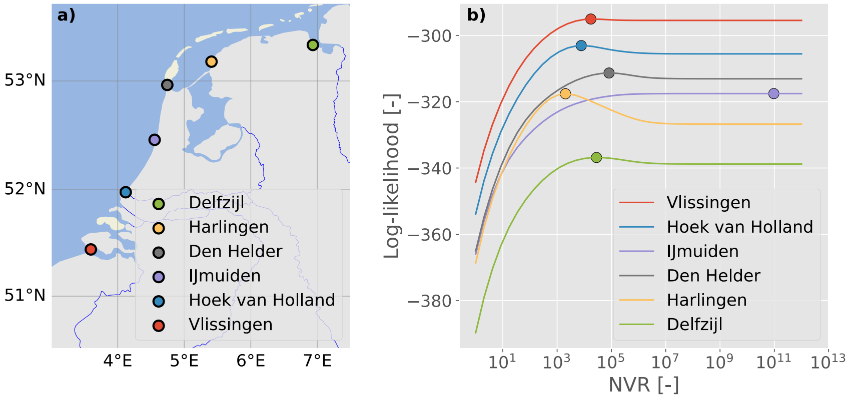

Figure 7. (a) Location of the six main Dutch tide gauge stations. (b) Comparison of the log-likelihood functions for the individual tide gauges as a function of the noise variance ratio (NVR $= \sigma_\epsilon^2/\sigma_\eta^2$). The colored dots indicate the value that was found by the numerical optimizer.

To assess the robustness of the MLE fit, we examine the log-likelihood functions while keeping the estimated observation variance and AR(1) parameter fixed, varying only the disturbance variance for the IRW trend. The resulting log-likelihood functions are shown in Figure 7. With the exception of Harlingen and Delfzijl, most stations do not exhibit a well-defined optimum, as indicated by the flat log-likelihood functions, which is particularly striking considering that the x-axis spans 12 orders of magnitude. Notably, the log-likelihood function for IJmuiden is entirely flat at its maximum, causing the numerical optimization algorithm to assign a very large value to the noise variance ratio, even though significantly smaller values yield nearly identical likelihoods. Excluding IJmuiden, the noise variance ratios for Harlingen and Den Helder still differ by two orders of magnitude. Note that the flattening of the log-likelihood functions occurs at NVRs of $\sim 10^6$, similar to the point at which the cut-off frequency levels off in Figure 5. This explains why the log-likelihood flattens: the width of the frequency response approaches the frequency resolution imposed by the length of the observation record.

The impact of the different fitted NVRs on the estimated trends is most clearly seen by comparing the frequency responses of the fitted models, which directly reveal how the trends at different stations are composed of different frequency components. We assume that the deterministic nodal cycle has minimal spectral overlap with the IRW trend, allowing us to disregard their interaction in the frequency response. However, since the errors are modeled as an AR(1) process, we cannot simply use the frequency response given in Equation 35. Deriving the frequency response for the IRW trend with AR(1) errors requires incorporating the structure of the non-diagonal observation covariance matrix. For details on this derivation, see Appendix C.

In Figure 8, the windowed frequency responses corresponding to the maximum likelihood parameters for IJmuiden, Den Helder and Harlingen are shown. Notably, all frequency responses approach zero at the frequency of the nodal cycle, confirming that the periodic component has minimal spectral overlap with the IRW trend component, and that their interaction can indeed be ignored. This also indicates that energy at the nodal cycle does not contribute to the IRW trends. However, variability associated with the Atlantic Multidecadal Oscillation (AMO), with a period of 50–70 years (Frankcombe et al., 2010; Mann et al., 2021), is mostly retained in the estimated trend at Harlingen, whereas it is largely filtered out for IJmuiden and Den Helder. Consequently, this creates an inconsistency in what the trends at the different stations represent. Still, there may also be physical explanations for sea level variability occurring at different timescales across the stations. For example, the smaller NVR at Harlingen might be partially due to sea level changes associated with the closure of the Zuiderzee between 1927 and 1932 and associated morphological adjustments.

The frequency responses can be used to guide the selection of the noise variances of the state space model, similar to their use in signal processing. For instance, one could set the cut-off frequency at the high-frequency boundary of the AMO variability if it is believed that such multi-decadal variability should be reflected in the sea level trend. However, given the multiple reasonable choices available, we advocate for an alternative approach: the state space models should be used with a range of plausible NVR values, allowing for an evaluation of how sensitive the conclusions are to these varying NVRs.

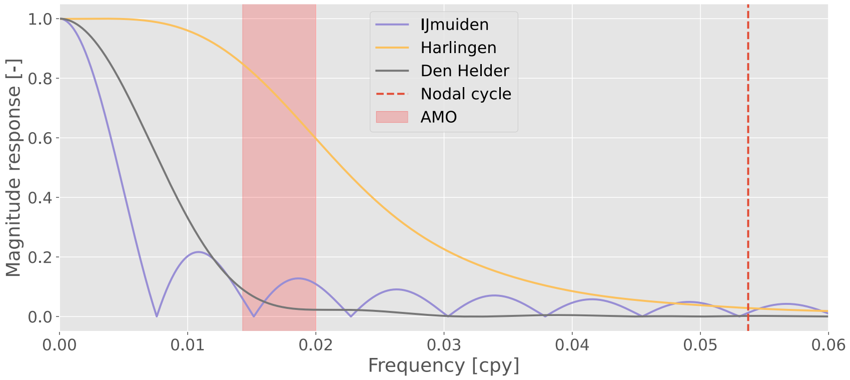

Figure 8. Windowed frequency responses for the integrated random walk trend with AR(1) errors corresponding to noise variance ratios of $2.3 \cdot 10^3$ (Harlingen), $1.1 \cdot 10^5$ (Den Helder) and $3.7 \cdot 10^{11}$ (IJmuiden) that were estimated using maximum likelihood. The red dashed vertical line indicates the frequency of the lunar nodal cycle. The frequency range of the Atlantic Multidecadal Oscillation (AMO) is given by the red shading.

To illustrate this, we compute sea level trends for NVRs between $2.2 \cdot 10^3$ and $2.5 \cdot 10^4$, covering cut-off frequencies corresponding to periods between 30 and 100 years. Subsequently, we compute the mean trends before and after 1993, a year that has recently been considered to be a breakpoint in rate of sea level rise in the North Sea (Steffelbauer et al., 2022; Stolte et al., 2023). In Figure 9, the blue and red lines represent the mean trends before and after 1993, respectively. If the red line exceeds the blue line, it suggests an acceleration in sea level rise. The red confidence intervals are considerably wider than the blue ones because the post-1993 trend is estimated over fewer time steps. Additionally, significant autocorrelation in the errors of the smoothed trend at short time lags further reduces the effective sample size, which increases uncertainty in the trend estimate.

At IJmuiden and Hoek van Holland, little to no acceleration is observed. An acceleration is likely at Vlissingen and Den Helder, although the confidence intervals for the trends before and after 1993 overlap. Finally, the acceleration appears most significant at Harlingen and Delfzijl, which is in line with findings from dedicated studies on sea level rise in the North Sea (Keizer et al., 2023; Steffelbauer et al., 2022).

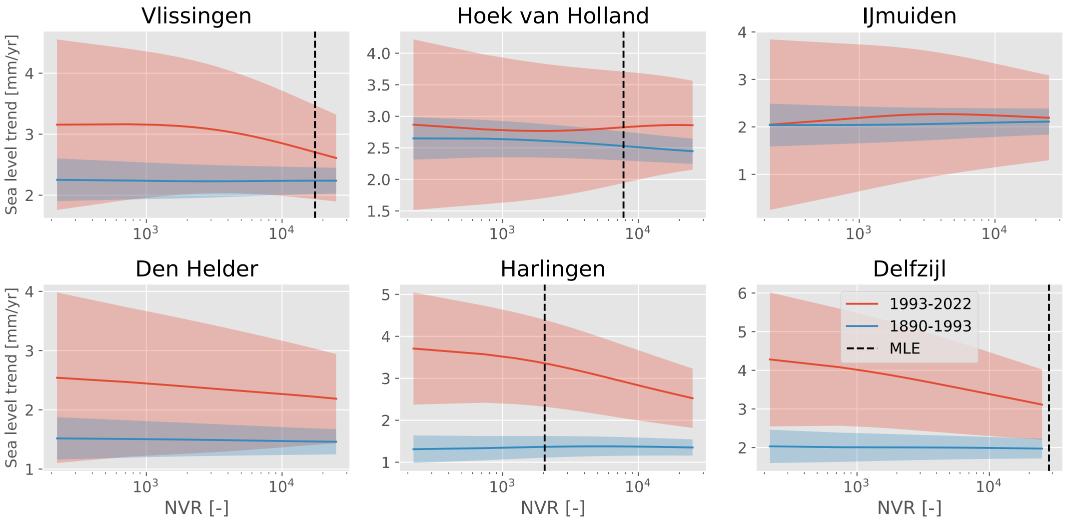

Figure 9. Estimated sea level trends as a function of the noise variance ratio (NVR = $\sigma_\varepsilon^2/\sigma_\eta^2$). The red lines denote the mean trend from 1993 until 2021, while the blue lines represent the mean trends from 1890 until 1992. Shaded regions indicate 95% confidence intervals. The vertical dashed black line denotes the maximum likelihood estimate (MLE) of the NVR. For IJmuiden and Den Helder, the maximum likelihood estimates of the NVR are not shown since they lie outside the range of considered NVRs (see Figure 7b).

6. Discussion and Conclusions

We have derived the frequency response of several state space models that are commonly used in time series analysis. The frequency response of a state space model is fully determined by the ratio between the observation and disturbance variances. We have demonstrated that it provides valuable insights into state space models and can guide informed choices for setting noise variance parameters.

This study extends existing frequency domain analyses of state space models by considering the actual solution to the smoothing problem, rather than focusing solely on the power spectral density of the transition equations. Moreover, we have discussed practical implications arising by finite observation records, which impose a lower bound on the attainable width of the frequency response. This finding explains the observed flattening of the log-likelihood function at large values of the noise variance ratio.

The main limitation of frequency response analysis is that a frequency response is only well-defined for linear time-invariant systems. Although many models in time series analysis are time-invariant, there are situations where a state space model may become time-varying.

One such case arises with irregular sampling. Although our analysis has focused on uniformly sampled data, deviations from this assumption, such as missing observations or alternating sampling patterns (e.g., at satellite crossover points), make the state space model time-varying. Still, we have observed (though not shown here) that the frequency response derived under uniform sampling often remains a useful approximation when such deviations are small.

Another source of time-variability is heteroskedasticity in the observation errors, which can limit the applicability of frequency response analysis. In contrast, colored but stationary observation noise does not pose the same issue. While we have primarily focused on models with white noise, the framework remains applicable to cases with stationary colored noise, such as the model with AR(1) observation noise discussed in Appendix C. In such cases, the system remains time-invariant, and frequency response analysis continues to be a valid and informative tool.

Additionally, our analysis has focused exclusively on univariate time series. In principle, the methodology could be extended to the multivariate setting. In the most general case, this would correspond to a multiple-input, multiple-output system, resulting in a distinct frequency response for each input-output pair. Consequently, the number of frequency responses would increase rapidly as the number of time series grows. Moreover, the derivation requires inversion of the observation and disturbance covariance matrices, which becomes tedious in the case of large full covariance matrices. In that case, it may be more appropriate to compute the frequency response for each input-output pair numerically by applying the state space filter to a large set of white noise realizations and computing the mean over the amplitude spectra of the outputs.

Finally, we have derived the frequency response only for the smoothing problem, not for the filtering problem. The frequency response of the Kalman filter could, in principle, be obtained by analytically computing the steady-state Kalman gain and applying the Z-transform to the recursive filtering equations. In general, the resulting magnitude response has a similar shape but exhibits a broader spectral width for the same noise variance ratio. A key difference, however, is that the phase response of the Kalman filter is nonzero, introducing phase distortions that are absent in the smoothing case.

Overall, the frequency response provides valuable insight into how the noise variance parameters affect state space models. It highlights which frequencies contribute to the estimated signals, reveals distinguishing spectral features of competing models, and helps understand the flat shape of the log-likelihood function for large noise variance ratios. Therefore, frequency response analysis serves as an important tool to help researchers make more informed decisions when applying state space models in time series analysis.

Appendix A: Derivation Frequency Response: Periodic Component With IRW Amplitudes

We consider the state space model consisting of a periodic component whose amplitudes are modeled as integrated random walks:

$$\begin{aligned} y_k &= a_k \cos(\omega_0 t_k) + b_k \cos(\omega_0 t_k) + \varepsilon_k, & \varepsilon_k &\sim N\left(0, \sigma_\varepsilon^2\right), \\ a_{k+1} &= 2a_k - a_{k-1} + \eta_k, & \eta_k, \eta_k^* &\sim N\left(0, \sigma_\eta^2\right), \\ b_{k+1} &= 2b_k - b_{k-1} + \eta_k^*. \end{aligned} \tag{A1}$$

Following the notation introduced in Section 2.2, we set:

$$\mathbf{x}_k = \begin{bmatrix} a_k & b_k \end{bmatrix}^\top, \tag{A2}$$

$$\mathbf{H}_k = \begin{bmatrix} \cos(\omega_0 t_k) & \sin(\omega_0 t_k) \end{bmatrix}, \tag{A3}$$

$$\mathbf{F}_k = \begin{bmatrix} 2 & 0 \\ 0 & 2 \end{bmatrix}, \tag{A4}$$

$$\mathbf{G}_k = \begin{bmatrix} -1 & 0 \\ 0 & -1 \end{bmatrix}. \tag{A5}$$

Substitution of the above matrices into Equation 21 yields the following system of difference equations:

$$\begin{gathered} r\hat{a}_{k-2} - 4r\hat{a}_{k-1} + \left(6r + \cos^2(\omega_0 t_k)\right) \hat{a}_k + \cos(\omega_0 t_k) \sin(\omega_0 t_k) \hat{b}_k \\ - 4r\hat{a}_{k+1} + r\hat{a}_{k+2} = \cos(\omega_0 t_k) y_k, \end{gathered} \tag{A6}$$

$$\begin{gathered} r\hat{b}_{k-2} - 4r\hat{b}_{k-1} + \left(6r + \sin^2(\omega_0 t_k)\right) \hat{b}_k + \cos(\omega_0 t_k) \sin(\omega_0 t_k) \hat{a}_k \\ - 4r\hat{b}_{k+1} + r\hat{b}_{k+2} = \sin(\omega_0 t_k) y_k. \end{gathered} \tag{A7}$$

Note that some of the coefficients are time-varying. In order to transform the system into a system with constant coefficients, we start by taking two linear combinations of the equations. First, multiply Equation A6 by $\cos(\omega_0 t_k)$, Equation A7 by $\sin(\omega_0 t_k)$ and sum the resulting equations. Second, multiply Equation A6 by $\sin(\omega_0 t_k)$, Equation A7 by $\cos(\omega_0 t_k)$ and subtract the second equation from the first equation. This yields the following system:

$$\begin{gathered} \hat{a}_k \cos(\omega_0 t_k) + \hat{b}_k \sin(\omega_0 t_k) \\ + r\left[\cos(\omega_0 t_k)\left(\nabla^4 \hat{a}_k\right) + \sin(\omega_0 t_k)\left(\nabla^4 \hat{b}_k\right)\right] = y_k, \end{gathered} \tag{A8}$$

$$\sin(\omega_0 t_k)\left(\nabla^4 \hat{a}_k\right) - \cos(\omega_0 t_k)\left(\nabla^4 \hat{b}_k\right) = 0. \tag{A9}$$

Note that this equations contains terms where the amplitude and trigonometric function correspond to different time steps, such as $\hat{a}_{k-1} \cos(\omega t_k)$. The trigonometric sum and difference formulas can be used to rewrite these terms to involve products evaluated at the same time step, for example:

$$\hat{a}_{k-1} \cos(\omega t_k) = \hat{a}_{k-1} \cos(\omega(t_{k-1} + \Delta t)) \tag{A10}$$

$$= \hat{a}_{k-1} \cos(\omega t_{k-1}) \cos(\omega \Delta t) - \hat{a}_{k-1} \cos(\omega t_{k-1}) \cos(\omega \Delta t) \tag{A11}$$

Thereafter, the transformation of variables defined in Equations 37 and 38 can again be used. Ultimately, this leads to transforming the system with time-varying coefficients into the following system with constant coefficients:

$$\begin{gathered} \hat{c}_k + r\left[\cos(2\tilde{\omega}_0)\left(\hat{c}_{k-2} + \hat{c}_{k+2}\right) + \sin(2\tilde{\omega}_0)\left(\hat{c}_{k-2}^* - \hat{c}_{k+2}^*\right) \right. \\ \left. - 4\cos(\tilde{\omega}_0)\left(\hat{c}_{k-1} + \hat{c}_{k+1}\right) - 4\sin(\tilde{\omega}_0)\left(\hat{c}_{k-1}^* - \hat{c}_{k+1}^*\right) + 6\hat{c}_k\right] = y_k, \end{gathered} \tag{A12}$$

$$\begin{aligned}&\cos(2\tilde{\omega}_0)[-\hat{c}^*_{k-2}-\hat{c}^*_{k+2}]+\sin(2\tilde{\omega}_0)\,[\hat{c}_{k-2}-\hat{c}_{k+2}]\\&-4\cos(\tilde{\omega}_0)[-\hat{c}^*_{k-1}-\hat{c}^*_{k+1}]-4\sin(\tilde{\omega}_0)\,[\hat{c}_{k-1}-\hat{c}_{k+1}]-6\hat{c}^*_k=0.\end{aligned}\tag{A13}$$

The homogeneity of the second equation again allows us to relate the Z-transform of $\hat{c}_k$ and $\hat{c}^*_k$, which is used to eliminate one of the variables from the Z-transform of the first equation. The frequency response can be derived using the steps outlined before and is given by:

$$H\left(e^{j\omega}\right)=\frac{1}{1+r\left[\frac{U(\omega)}{V(\omega)}-V(\omega)\right]},\tag{A14}$$

where

$$\begin{aligned}U(\omega)=\;&\sin^2(2\tilde{\omega}_0)(2-2\cos(4\omega))\\&-16\sin(\tilde{\omega}_0)\sin(2\tilde{\omega}_0)(\cos(\omega)-\cos(3\omega))\\&-16\sin^2(\tilde{\omega}_0)(2\cos(2\omega)-2)),\end{aligned}\tag{A15}$$

$$V(\omega)=8\cos(\tilde{\omega}_0)\cos(\omega)-2\cos(2\tilde{\omega}_0)\cos(2\omega)-6.\tag{A16}$$

Appendix B: Derivation Frequency Response: Sum of IRW Trend and RW Cycle

Here we consider the derivation of the frequency responses of a model consisting of two stochastic components: an IRW trend an a cylic component with random walk amplitudes. We thus consider the following model:

$$\begin{aligned}y_k&=\mu_k+c_k+\varepsilon_k, &\varepsilon_k&\sim N\left(0,\sigma^2_\varepsilon\right),\\ \mu_{k+1}&=2\mu_k-\mu_{k-1}+\eta_k, &\eta_k&\sim N\left(0,\sigma^2_\eta\right),\\ c_{k+1}&=\cos(\tilde{\omega}_0)\,c_k+\sin(\tilde{\omega}_0)\,c^*_k+\xi_k, &\xi_k,\xi^*_k&\sim N\left(0,\sigma^2_\xi\right),\\ c^*_{k+1}&=-\sin(\tilde{\omega}_0)\,c_k+\cos(\tilde{\omega}_0)\,c^*_k+\xi^*_k.\end{aligned}\tag{B1}$$

We set $\mathbf{x}_k=\begin{bmatrix}\mu_k & c_k & c^*_k\end{bmatrix}^\top$, $\mathbf{H}_k=\begin{bmatrix}1 & 1 & 0\end{bmatrix}$ and

$$\mathbf{F}_k=\begin{bmatrix}2 & 0 & 0\\ 0 & \cos(\omega_0t_k) & \sin(\omega_0t_k)\\ 0 & -\sin(\omega_0t_k) & \cos(\omega_0t_k)\end{bmatrix},\tag{B2}$$

$$\mathbf{G}_k=\begin{bmatrix}-1 & 0 & 0\\ 0 & 0 & 0\\ 0 & 0 & 0\end{bmatrix}.\tag{B3}$$

Substitution of the above matrices into Equation 21 now yields the following system of difference equations:

$$\hat{\mu}_k+r_\eta\nabla^4\hat{\mu}_k+\hat{c}_k=y_k,\tag{B4}$$

$$\begin{aligned}&-r_\xi\cos(\tilde{\omega}_0)\,[\hat{c}_{k-1}+\hat{c}_{k+1}]-r_\xi\sin(\tilde{\omega}_0)\,[\hat{c}^*_{k-1}-\hat{c}^*_{k+1}]\\&+(1+2r_\xi)\,\hat{c}_k+\hat{\mu}_k=y_k,\end{aligned}\tag{B5}$$

$$\sin(\tilde{\omega}_0)\,[\hat{c}_{k-1}-\hat{c}_{k+1}]-\cos(\tilde{\omega}_0)\,[\hat{c}^*_{k-1}+\hat{c}^*_{k+1}]+2\hat{c}^*_k=0,\tag{B6}$$

where we now have two noise variance ratios:

$$r_\eta = \frac{\sigma_\varepsilon^2}{\sigma_\eta^2}, \qquad r_\xi = \frac{\sigma_\varepsilon^2}{\sigma_\xi^2}. \tag{B7}$$

The first equation still contains three variables: $\hat{\mu}_k$, $\hat{c}_k$ and y_k, so we need to eliminate one to relate two of their Z-transforms. We can subtract Equation B5 from Equation B4 to eliminate y_k. This yields:

$$\begin{gathered} r_\eta \nabla^4 \hat{\mu}_k + r_\xi \cos(\tilde{\omega}_0)\left[\hat{c}_{k-1} + \hat{c}_{k+1}\right] \\ + r_\xi \sin(\tilde{\omega}_0)\left[\hat{c}^*_{k-1} - \hat{c}^*_{k+1}\right] - 2 r_\xi \hat{c}_k = 0. \end{gathered} \tag{B8}$$

Taking the Z-transform of the above equation gives:

$$\begin{gathered} M(z) r_\eta \left[z^{-2} - 4z^{-1} + 6 - 4z + z^2\right] + C(z) r_\xi \left[\cos(\tilde{\omega}_0)\left(z^{-1} + z\right) - 2\right] \\ + C^*(z) r_\xi \left[\sin(\tilde{\omega}_0)\left(z^{-1} - z\right)\right] = 0, \end{gathered} \tag{B9}$$

where $C(z) = \mathcal{Z}\{\hat{c}[k]\}$ and $C^*(z) = \mathcal{Z}\{\hat{c}^*[k]\}$. $C^*(z)$ can be eliminated by relating it to $C(z)$ after Z-transforming Equation B6, which yields

$$r_\xi D(z) C(z) = r_\eta \nabla^4(z) M(z), \tag{B10}$$

where

$$D(z) = \cos(\tilde{\omega}_0)\left(z^{-1} + z\right) - 2 + \frac{\sin^2(\tilde{\omega}_0)\left(z^{-1} - z\right)\left(z - z^{-1}\right)}{2 - \cos(\tilde{\omega}_0)\left(z^{-1} + z\right)}, \tag{B11}$$

$$\nabla^4(z) = -z^{-2} + 4z^{-1} - 6 + 4z - z^2. \tag{B12}$$

Note that as this model contains two stochastic components, there will also be two transfer functions, that is,

$$H_C(z) = \frac{C(z)}{Y(z)}, \tag{B13}$$

$$H_M(z) = \frac{M(z)}{Y(z)}. \tag{B14}$$

To find $H_C(z)$, we express $M(z)$ as a function of $C(z)$ by reordering Equation B10. This expression can be substituted into the Z-transform of Equation B4 which yields an equation consisting only of $C(z)$ and $Y(z)$, which can thus be reordered to find the transfer function for the periodic component. Conversely, to find $H_M(z)$, we express $C(z)$ as a function of $M(z)$ and follow the same steps. This yields the following two frequency responses for the trend and cyclic term respectively:

$$H_M\left(e^{j\omega}\right) = \frac{M\left(e^{j\omega}\right)}{Y\left(e^{j\omega}\right)} = \frac{1}{1 + r_\eta\left[\frac{\nabla^4\left(e^{j\omega}\right)}{r_\xi D\left(e^{j\omega}\right)} - \nabla^4\left(e^{j\omega}\right)\right]}, \tag{B15}$$

$$H_C\left(e^{j\omega}\right) = \frac{C\left(e^{j\omega}\right)}{Y\left(e^{j\omega}\right)} = \frac{1}{1 + r_\xi\left[\frac{D\left(e^{j\omega}\right)}{r_\eta \nabla^4\left(e^{j\omega}\right)} - D\left(e^{j\omega}\right)\right]}. \tag{B16}$$

Appendix C: Derivation Frequency Response: IRW Trend With AR(1) Errors

Here we consider the derivation of the frequency response of the state space model consisting of an IRW trend and AR(1) errors, that is,

$$\begin{aligned} y_k &= \mu_k + \varepsilon_k, & & \\ \mu_{k+1} &= 2\mu_k - \mu_{k-1} + \eta_k, & \eta_k &\sim N\left(0,\sigma_\eta^2\right), \\ \varepsilon_{k+1} &= \phi\varepsilon_k + \xi_k, & \xi_k &\sim N\left(0,\sigma_\xi^2\right), \end{aligned} \tag{C1}$$

Compared to the derivation in Section 3.2, we now need to account for the AR(1) structure of the observation errors. The observation covariance matrix is given by:

$$\mathbf{R} = \sigma_\varepsilon^2 \begin{bmatrix} 1 & \phi & \phi^2 & \dots & \phi^{N-1} \\ \phi & 1 & \phi & \dots & \phi^{N-2} \\ \phi^2 & \phi & 1 & \dots & \phi^{N-3} \\ \vdots & \vdots & \vdots & \ddots & \vdots \\ \phi^{N-1} & \phi^{N-2} & \phi^{N-3} & \dots & 1 \end{bmatrix}. \tag{C2}$$

To find the difference equations, we need $\mathbf{R}^{-1}$, given by the following tridiagonal matrix:

$$\mathbf{R}^{-1} = \frac{1}{\sigma_\varepsilon^2\left(1-\phi^2\right)} \begin{bmatrix} 1 & -\phi & 0 & \cdots & 0 \\ -\phi & 1+\phi^2 & -\phi & \cdots & 0 \\ 0 & -\phi & 1+\phi^2 & \cdots & 0 \\ \vdots & \vdots & \vdots & \ddots & -\phi \\ 0 & 0 & 0 & -\phi & 1 \end{bmatrix}. \tag{C3}$$

Note that we do not consider ε_k to be a state. Hence, the observation and transition matrices are the same as in the IRW trend case. Then, we can substitute $\mathbf{R}^{-1}$ into Equation 10 to find the following difference equation:

$$r\hat{\mu}_{k-2} + (a-4r)\hat{\mu}_{k-1} + (b+6r)\hat{\mu}_k + (a-4r)\hat{\mu}_{k+1} + r\hat{\mu}_{k+2} = ay_{k-1} + by_k + ay_{k+1}, \tag{C4}$$

where

$$a = \frac{-\phi}{1-\phi^2}, \tag{C5}$$

$$b = \frac{1+\phi^2}{1-\phi^2}. \tag{C6}$$

Compared to the difference equation for the IRW trend with uncorrelated observation errors (Equation 34), the major difference is the direct dependence on y_{k-1} and y_{k+1}. The frequency response can again be found via the Z-transform, which ultimately yields:

$$H\left(e^{j\omega}\right) = \frac{2a\cos(\omega) + b}{b + r(6 + 2\cos(2\omega)) + 2(b-4r)\cos(\omega)}. \tag{C7}$$

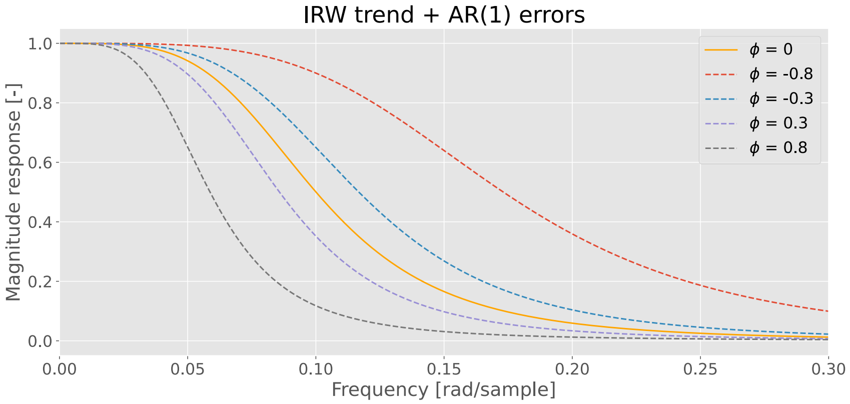

Figure C1. Frequency response of state space model consisting of an integrated random walk (IRW) trend and AR(1) observation errors for different values of the AR(1) parameter ϕ. The noise variance ratio is fixed at $r = 10^4$.

In Figure C1, the frequency response is visualized for several values of ϕ. For $\phi = 0$, the frequency response reduces to Equation 35. For values of $\phi < 0.3$, the change in frequency response is quite small. However, the differences are quite considerable for large values of ϕ.

Appendix D: Connection With the Wiener Filter

The frequency response of the non-causal discrete-time Wiener filter is given by (Equation 12.33, Oppenheim & Verghese, 2015):

$$H\left(e^{j\omega}\right) = \frac{S_{xy}}{S_{yy}}, \tag{D1}$$

where S_{xy} is the cross-spectral density between observations y and states x, and S_{yy} is the power spectral density (PSD) of the observations. This filter is optimal in the mean squared error sense when x and y are jointly wide-sense stationary (Oppenheim & Verghese, 2015). Although the signals considered in this paper are clearly non-stationary (e.g., the variance of an RW scales linearly in time), the frequency responses for the Wiener filter and Kalman smoother still coincide. As an example, consider the RW model, whose PSD is given by (Equation 2.4.51; Harvey, 1990):

$$S_{xx} = \frac{\sigma_\eta^2}{2 - 2\cos(\omega)} \tag{D2}$$

Since x_k and ε_k are uncorrelated, it follows that $S_{xy} = S_{xx}$ and $S_{yy} = S_{xx} + \sigma_\varepsilon^2$. Thus, by Equation D1, we have

$$H\left(e^{j\omega}\right) = \frac{S_{xx}}{S_{xx} + \sigma_\varepsilon^2} \tag{D3}$$

$$= \frac{\frac{\sigma_\eta^2}{2-2\cos(\omega)}}{\frac{\sigma_\eta^2}{2-2\cos(\omega)} + \sigma_\varepsilon^2} \tag{D4}$$

$$= \frac{1}{1 + r[2 - 2\cos(\omega)]}, \tag{D5}$$

which matches exactly the expression in Equation 27. This equivalence holds for all models considered in this paper. Hence, we conclude that although the conditions for optimality of the Wiener filter are not met, it still yields the same frequency response as the Kalman smoother.

Conflict of Interest

The authors declare no conflicts of interest relevant to this study.

Data Availability Statement

The PSMSL data (PSMSL, 2025) can be found at http://www.psmsl.org/data/obtaining/. The GTSM data are from Stolte et al. (2023), and can be found at https://github.com/openearth/sealevel/tree/report/data/deltares/gtsm. All scripts to produce the figures and analysis throughout this paper are available at the associated GitHub repository: https://github.com/khaakman/state-space-frequency-response, and archived with a DOI at Zenodo: https://doi.org/10.5281/zenodo.17378609.

Acknowledgments

Koen Haakman is funded through the Dutch Research Council (NWO) under Grant number ENW.GO.001.011. The authors thank Frithjof Ehlers, Roland Klees and Taco Broerse for helpful discussions about the subject.

References

Aravkin, A. Y., Burke, J. V., & Pillonetto, G. (2014). Optimization viewpoint on Kalman smoothing with applications to robust and sparse estimation. In A. Y. Carmi, L. Mihaylova, & S. J. Godsill (Eds.), *Compressed sensing & sparse filtering* (pp. 237–280). Springer Berlin Heidelberg. https://doi.org/10.1007/978-3-642-38398-4_8

Auger-Méthé, M., Field, C., Albertsen, C. M., Derocher, A. E., Lewis, M. A., Jonsen, I. D., & Mills Flemming, J. (2016). State-space models' dirty little secrets: Even simple linear Gaussian models can have estimation problems. *Scientific Reports*, *6*(1), 26677. https://doi.org/10.1038/srep26677

Chopin, N., & Papaspiliopoulos, O. (2020). Maximum likelihood estimation of state-space models. In *An introduction to sequential Monte Carlo* (pp. 251–277). Springer International Publishing. https://doi.org/10.1007/978-3-030-47845-2_14

Davis, J. L., Wernicke, B. P., & Tamisiea, M. E. (2012). On seasonal signals in geodetic time series. *Journal of Geophysical Research*, *117*(B1). https://doi.org/10.1029/2011JB008690

Durbin, J., & Koopman, S. J. (2012). *Time series analysis by state space methods* (2nd ed.). Oxford University Press. https://doi.org/10.1093/acprof:oso/9780199641178.001.0001

Fox-Kemper, B., Hewitt, H., Xiao, C., Aðalgeirsdóttir, G., Drijfhout, S., Edwards, T., et al. (Eds.), Climate change 2021: The physical science Basis. Contribution of Working Group I to the sixth assessment report of the intergovernmental Panel on climate change (pp. 1211–1362). https://doi.org/10.1017/9781009157896.011

Frankcombe, L. M., von der Heydt, A., & Dijkstra, H. A. (2010). North Atlantic multidecadal climate variability: An investigation of dominant time scales and processes. *Journal of Climate*, *23*(13), 3626–3638. https://doi.org/10.1175/2010JCLI3471.1

Frederikse, T., & Gerkema, T. (2018). Multi-decadal variability in seasonal mean sea level along the North Sea coast. *Ocean Science*, *14*(6), 1491–1501. https://doi.org/10.5194/os-14-1491-2018

Frederikse, T., Riva, R., Slobbe, C., Broerse, T., & Verlaan, M. (2016). Estimating decadal variability in sea level from tide gauge records: An application to the North Sea. *Journal of Geophysical Research: Oceans*, *121*(3), 1529–1545. https://doi.org/10.1002/2015JC011174

Harvey, A. C. (1990). *Forecasting, structural time series models and the Kalman filter*. Cambridge University Press.

Holgate, S. J., Matthews, A., Woodworth, P. L., Rickards, L. J., Tamisiea, M. E., Bradshaw, E., et al. (2013). New data systems and products at the permanent service for mean sea level. *Journal of Coastal Research*, *29*(3), 493–504. https://doi.org/10.2112/JCOASTRES-D-12-00175.1

Keizer, I., Le Bars, D., de Valk, C., Jüling, A., van de Wal, R., & Drijfhout, S. (2023). The acceleration of sea-level rise along the coast of the Netherlands started in the 1960s. *Ocean Science*, *19*(4), 991–1007. https://doi.org/10.5194/os-19-991-2023

Laine, M., Latva-Pukkila, N., & Kyrölä, E. (2014). Analysing time-varying trends in stratospheric ozone time series using the state space approach. *Atmospheric Chemistry and Physics*, *14*(18), 9707–9725. https://doi.org/10.5194/acp-14-9707-2014

Mann, M. E., Steinman, B. A., Brouillette, D. J., & Miller, S. K. (2021). Multidecadal climate oscillations during the past millennium driven by volcanic forcing. *Science*, *371*(6533), 1014–1019. https://doi.org/10.1126/science.abc5810

Muis, S., Verlaan, M., Winsemius, H. C., Aerts, J. C. J. H., & Ward, P. J. (2016). A global reanalysis of storm surges and extreme sea levels. *Nature Communications*, *7*(1), 11969. https://doi.org/10.1038/ncomms11969

Opel, L., Schindelegger, M., & Ray, R. D. (2024). A likely role for stratification in long-term changes of the global ocean tides. *Communications Earth and Environment*, *5*(1), 261. https://doi.org/10.1038/s43247-024-01432-5

Oppenheim, A. V., & Schafer, R. W. (1999). *Discrete-time signal processing* (2nd ed.). Prentice-Hall.

Oppenheim, A. V., & Verghese, G. C. (2015). *Signals, systems and inference*. Pearson.

Plasil, M. (2023). State space estimation: From Kalman filter back to least squares. *Statistika*, *103*(2), 235–245. https://doi.org/10.54694/stat.2023.3

Proietti, T. (2000). Comparing seasonal components for structural time series models. *International Journal of Forecasting*, *16*(2), 247–260. https://doi.org/10.1016/S0169-2070(00)00037-6

PSMSL. (2025). Tide gauge data [Dataset]. Retrieved from http://www.psmsl.org/data/obtaining/

Pugh, D., & Woodworth, P. (2014). *Sea-level science: Understanding tides, surges, tsunamis and mean sea-level changes*. Cambridge University Press.

Rauch, H. E., Tung, F., & Striebel, C. T. (1965). Maximum likelihood estimates of linear dynamic systems. *AIAA Journal*, *3*(8), 1445–1450. https://doi.org/10.2514/3.3166

Steffelbauer, D. B., Riva, R. E. M., Timmermans, J. S., Kwakkel, J. H., & Bakker, M. (2022). Evidence of regional sea-level rise acceleration for the North Sea. *Environmental Research Letters*, *17*(7), 074002. https://doi.org/10.1088/1748-9326/ac753a

Stolte, W., Baart, F., Muis, S., Hijma, M., Taal, M., Bars, D. L., & Drijfhout, S. (2023). *Zeespiegelmonitor 2022 (Tech. Rep. No. 11209266-000-ZKS-0001)*. Deltares. Retrieved from https://publications.deltares.nl/11209266_000.pdf

Visser, H., Dangendorf, S., & Petersen, A. C. (2015). A review of trend models applied to sea level data with reference to the "acceleration-deceleration debate". *Journal of Geophysical Research: Oceans*, *120*(6), 3873–3895. https://doi.org/10.1002/2015JC010716

Whittle, P. (1991). Likelihood and cost as path integrals. *Journal of the Royal Statistical Society: Series B*, *53*(3), 505–529. https://doi.org/10.1111/j.2517-6161.1991.tb01842.x

Willen, M. O., Broerse, T., Groh, A., Wouters, B., Kuipers Munneke, P., Horwath, M., et al. (2021). Separating long-term and short-term mass changes of Antarctic ice drainage basins: A coupled state space analysis of satellite observations and model products. *Journal of Geophysical Research: Earth Surface*, *126*(6), e2020JF005966. https://doi.org/10.1029/2020JF005966

Young, P. C., Pedregal, D. J., & Tych, W. (1999). Dynamic harmonic regression. *Journal of Forecasting*, *18*(6), 369–394. https://doi.org/10.1002/(SICI)1099-131X(199911)18:6<369::AID-FOR748>3.0.CO;2-K